Humic acid metal cation interaction studied by spectromicroscopy techniques in combination with quantum chemical calculations

M. Plaschke,[a]* J. Rothe,[a] M. K. Armbruster,[a] M. A. Denecke,[a] A. Naber[b] and H. Geckeis[a]

[a]Karlsruher Institut für Technologie (KIT), Institut für Nukleare Entsorgung, Hermann-von-Helmholtz-Platz 1, 76344 Eggenstein-Leopoldshafen, Germany, and [b]Karlsruher Institut für Technologie (KIT), Institut für Angewandte Physik, Wolfgang-Gaede-Strasse 1, 76131 Karlsruhe, Germany. E-mail: markus.plaschke@kit.edu

Humic acids (HA) have a high binding capacity towards traces of toxic metal cations, thus affecting their transport in aquatic systems. Eu(III)–HA aggregates are studied by synchrotron-based scanning transmission X-ray microscopy (STXM) at the carbon K-edge and laser scanning luminescence microscopy (LSLM) at the $^5D_0 \rightarrow {}^7F_{1,2}$ fluorescence emission lines. Both methods provide the necessary spatial resolution in the sub-micrometre range to resolve characteristic aggregate morphologies: optically dense zones embedded in a matrix of less dense material in STXM images correspond to areas with increased Eu(III) luminescence yield in the LSLM micrographs. In the C 1s-NEXAFS of metal-loaded polyacrylic acid (PAA), used as a HA model compound, a distinct complexation effect is identified. This effect is similar to trends observed in the dense fraction of HA/metal cation aggregates. The strongest complexation effect is observed for the Zr(IV)–HA/PAA system. This effect is confirmed by quantum chemical calculations performed at the *ab initio* level for model complexes with different metal centres and complex geometries. Without the high spatial resolution of STXM and LSLM and without the combination of molecular modelling with experimental results, the different zones indicating a 'pseudo'-phase separation into strong complexing domains and weaker complexing domains of HA would never have been identified. This type of strategy can be used to study metal interaction with other organic material.

1. Introduction

Humic acids (HA) left over from biodegradation of living organisms possess chemically reactive sites, which potentially regulate transport and retention of contaminants in aquifers, soils and sediments (Hayes, 1989). Owing to their inherent chemical heterogeneity and polydispersity, HA exhibit numerous interactions in the environment, including complexation of metal cations and coating of inorganic colloids like clays and iron oxide/hydroxides. Possible risks posed by organic macromolecules complexing and mobilizing toxic trace metal cations (M^{n+}), *e.g.* actinide cations in the case of nuclear waste disposal in geological formations (Kim, 1994), have been the subject of various research efforts in the past. Aquatic HA are commonly characterized as colloid-sized polyfunctional biopolymers with high structural diversity

depending on origin and formation history. So far, this diversity has been a limiting factor in the search for a unified structural model for HA. The role of proton-exchanging functional groups such as carboxylic or phenolic groups has been investigated by many researchers in order to describe HA complexation behaviour. Previous comparative EXAFS studies of HA and ion exchange resins point to carboxylate groups as the primary HA metal ion binding sites (Denecke *et al.*, 1998). Characterization of the number and density of these proton-exchanging groups is accessible by titration experiments. These values are correlated to the metal loading capacity, a key feature in the description of HA, according to the charge neutralization model (Kim & Czerwinski, 1996). However, the exact molecular structures of M^{n+}–HA complexes are generally unknown. Typical HA characteristics such as varying complexation strength (described in terms of

Table 1
Samples used for STXM and LSLM measurements.

Sample ID	[HA] or [PAA] (mg l^{-1})	[M^{n+}] (mol l^{-1})	pH
Na–PAA	–	–	Dried
Zr(IV)–PAA pH 3	100	1.1×10^{-3}	3.2
Zr(IV)–PAA pH 4	100	1.1×10^{-3}	4.0
Zr(IV)–PAA pH 5	100	1.1×10^{-3}	5.3
Zr(IV)–HA pH 4	100	1.1×10^{-3}	3.9
HA pH 4	100	–	4.3
Eu(III)–HA pH 5	100	3.0×10^{-3}	5.1

stability or complexation constants) or quasi-irreversible reaction kinetics observed for certain HA fractions (sometimes associated with binding by 'strong sites') are not well understood in macroscopic HA descriptions based on bulk characterization techniques.

The nature of M^{n+}–HA complexes has been investigated by laser excitation luminescence spectroscopy, where predominantly trivalent actinides [e.g. Cm^{3+} (Monsallier et al., 2003)] or chemical homologue lanthanides [e.g. Eu^{3+} (Monsallier et al., 2001)] with high luminescence yields act as sensitive probes reflecting the local coordination environment. However, for a detailed understanding of aggregation and metal ion complexation, specific information on the distribution of HA functional groups and their response to HA metal cation loading is mandatory.

Recently, the usefulness of carbon K-edge (C 1s-level at ~285 eV) NEXAFS (near-edge X-ray absorption fine structure) spectroscopy for investigation of M^{n+}–HA complexes from the point of view of the organic ligands has been demonstrated (Thieme et al., 2000; Myneni, 2002; Christl & Kretzschmar, 2007; Plaschke et al., 2004, 2005). C 1s-NEXAFS spectromicroscopy with sub-micrometre lateral resolution for in situ investigations of hydrated HA samples is available at scanning transmission X-ray microscopy (STXM) stations, e.g. at the NSLS (Brookhaven, NY, USA), ALS (Berkeley, CA, USA), SLS (Villigen, Switzerland) and CLS (Saskatoon, Canada) synchrotron light sources (Jacobsen et al., 1991; Bluhm et al., 2006; Tzvetkov et al., 2008; Kaznatcheev et al., 2007). Chemical speciation of HA using C 1s-NEXAFS provides information on structural subunits based on characteristic spectral features owing to C 1s → π*/σ* transition resonances, e.g. the carboxylic C 1s (COO$^-$) → π*$_{C=O}$ transition at ~288.4 eV (Hitchcock et al., 1992).

In the present paper we review results obtained from combined synchrotron- and laser-based spectromicroscopy methods with quantum chemical calculations to characterize the metal cation interaction with HA. From investigations conducted over the past decade utilizing a strategy of comparing results from metal cation/HA studies with those from metal interaction with well defined model systems (both molecular and polymeric), we have learned that comprehending the metal cation interaction with chemically heterogeneous and structurally ill-defined HA is only possible through the combination of high spatial resolution spectromicroscopies probing both ligand and metal cation with

quantum chemical molecular modelling. The aim of this paper is to convey the success of this strategy and combination of experiment with theory in advancing our understanding of metal–humic interaction with hopes that this might find a more general application to studies of metal binding to organic material.
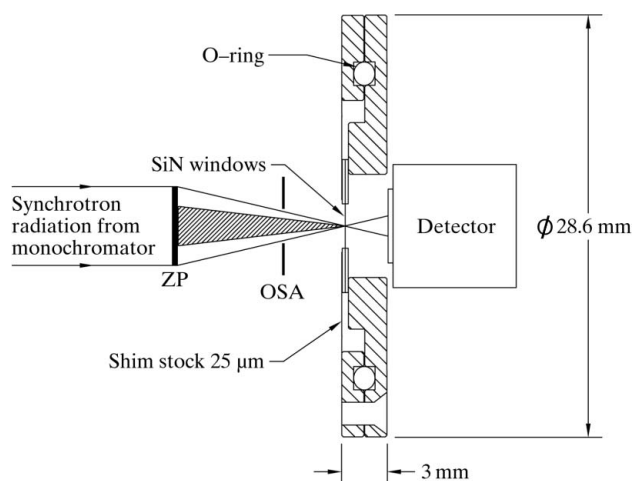
2. Materials and methods

2.1. Samples

All chemicals used in our spectromicroscopy studies were of analytical grade. In most cases commercially available Aldrich HA (Deisenhofen, Germany) was used as reference material. Aldrich HA was purified according to a procedure described by Kim and Buckau (Kim et al., 1990). A stock solution of 400 mg l^{-1} with an electrolyte content of 0.1 M NaCl was prepared, adjusted to pH ~5.0 and stored at 278 K. Polyacrylic acid (PAA: [–CH$_2$–CH(COOH)–]$_n$) has found widespread application to mimic HA in metal ion complexation studies (cf. Rothe et al., 2007a, and references therein). PAA is a water soluble polymer with a high content of carboxyl functional groups attached to an aliphatic chain. We have chosen PAA (GPC standard, Fluka, 60.000 Da) as an appropriate model compound in an attempt to clarify the role of carboxyl groups in the HA/metal ion interaction. Aqueous suspensions of HA and PAA, both at 100 mg l^{-1}, were contacted with polyvalent metal cations, e.g. Eu(III) (diluted ICP-MS standard), as a homologue for trivalent actinides such as Am(III), or Zr(IV) (diluted ICP-MS standard), as a homologue for tetravalent actinides such as Pu(IV). Final metal concentrations were chosen to saturate HA or PAA loading capacities and are summarized in Table 1. Addition of metal cations to HA and PAA or acidification of pure HA suspensions to pH 1 induced the polymers to flocculate and precipitate from solution, resulting in aggregates of adequate dimension and density to be probed by carbon K-edge spectromicroscopy and laser scanning luminescence microscopy (LSLM). Contact times between cation addition and measurements were 1–2 weeks. Aliquots of 2 μl from approximately 2 ml sample reaction volume were used for both STXM and LSLM studies.

2.2. STXM/C 1s-NEXAFS

STXM investigations were performed at beamline X-1A (outboard STXM) at the NSLS, Brookhaven National Laboratory, NY, USA (Jacobsen et al., 2000). At this experimental station, a Fresnel zone plate is used to focus soft X-rays provided by the NSLS synchrotron source into a spot of width less than 100 nm. The spherical grating monochromator is calibrated against the C 1s-absorption threshold resonance of carbon dioxide at 292.76 eV. An energy resolution of ~0.1 eV is achieved. Samples are raster-scanned across the focused beam while recording the transmitted intensity by a proportional counter. Stacks of images from selected sample regions are obtained as a function of incident photon energy, E. C 1s-NEXAFS spectra are extracted through the analysis of

soil and geosciences

the absorption signal, $\mu(E)d = \ln[I_0(E)/I_C(E)]$, of vertical projections onto aligned image stacks. Image regions free of condensed carbonaceous material supply information on the I_0 signal. This method is justified as we never succeeded to derive useful C 1s-NEXAFS signals from dissolved carbon species. The transmitted intensity (I_C) is derived from image regions containing carbonaceous aggregates, *i.e.* regions with a strong absorption contrast to the surrounding water film. Minor spectral distortions owing to non-flocculated HA in the water film cannot be fully excluded. However, they are definitely of minor relevance compared with possible distortions owing to carbon deposits on beamline optical elements. A schematic representation of the STXM set-up is shown in Fig. 1 (image taken from Neuhäusler *et al.*, 2000). HA and PAA suspensions were investigated in the fully hydrated state, sandwiched between two silicon nitride membranes (thickness 100 nm). Details on wet cell sample preparation and stack data analysis can be found by Jacobsen *et al.* (2000).

2.3. LSLM

The Eu(III) distribution in Eu(III)–HA aggregates was mapped by means of LSLM. Since the luminescence yield of lanthanide ions is low compared with good fluorophores like organic dyes, the application of advanced optical detection techniques was indispensable. We used a home-built LSLM based on an inverse optical microscope (Nikon TE2000-U) equipped with a piezoelectric sample scanning stage (Fig. 2). In this set-up the Eu(III) luminescence is collected by an avalanche photodiode using different emission filters with the centre wavelength set to typical HA luminescence emission (565 nm) and the two dominant Eu(III) emission lines ($^5D_0 \rightarrow {}^7F_1$ at 592 nm and $^5D_0 \rightarrow {}^7F_2$ at 615 nm). For luminescence excitation of Eu(III), the light of a blue diode laser (DL-SHG 110, Toptica, Germany) is guided to the microscope *via* a single-mode optical fibre and focused through the microscope objective to form a diffraction limited spot of width about
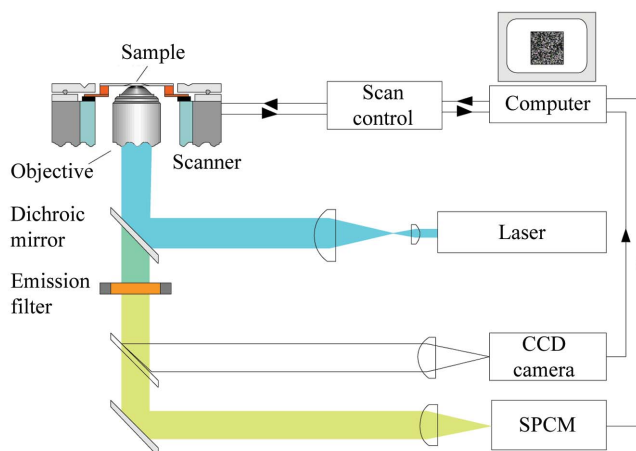
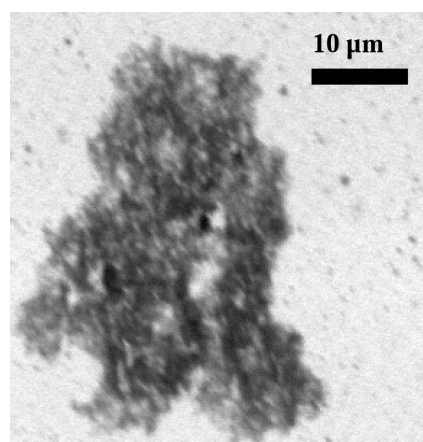200 nm on the sample. The laser wavelength is fine-tuned to the maximum of a narrow absorption line of Eu(III) ($^7F_0 \rightarrow {}^5L_6$ excitation at λ = 393.5 nm). Aqueous Eu(III)–HA suspensions were investigated as thin films enclosed between two cleaned microscope cover slides (*cf.* Naber *et al.*, 2006 for details).
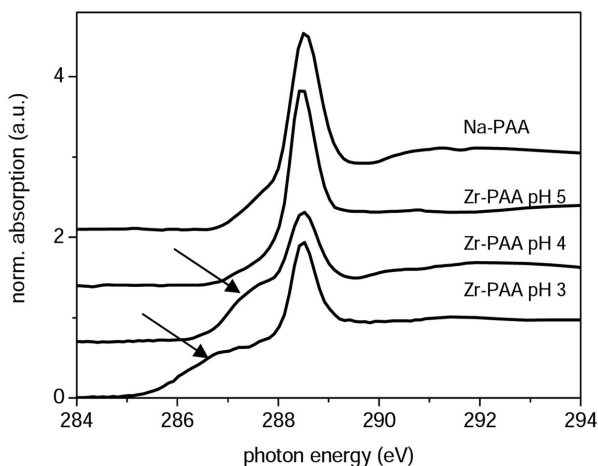
3. Results and discussion

3.1. Spectromicroscopy results

A typical STXM micrograph of precipitated Zr(IV)–PAA imaged in fully hydrated state at pH 5 is shown in Fig. 3. Metal-loaded PAA aggregates exhibit uniform C 1s-NEXAFS spectra, pointing to the chemical homogeneity of the material. The NEXAFS spectrum strongly depends on the solution pH (Fig. 4). At pH 5 and higher we observe the spectrum of uncomplexed PAA, similar to the NEXAFS of Na–PAA (Plaschke *et al.*, 2004). At pH 4 the decrease of the carboxyl
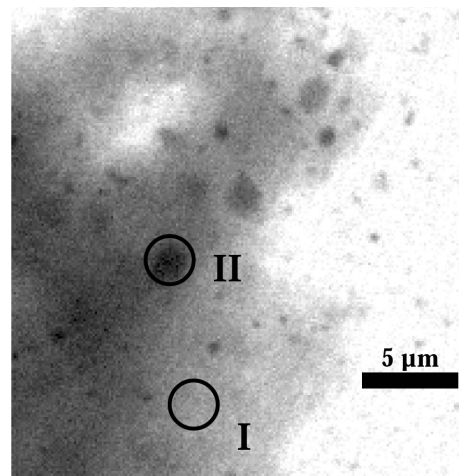
Figure 4
Normalized C 1s-NEXAFS for Na–PAA and Zr(IV)–PAA at different pH ([Zr(IV)] = 1.1 × 10⁻³ mol l⁻¹); figure reprinted from Rothe *et al.* (2007*b*), with permission from the American Institute of Physics; copyright 2007.

Figure 5
STXM micrograph of Zr(IV)–HA (pH 4) recorded at 288.4 eV ([Zr(IV)] = 1.1 × 10⁻³ mol l⁻¹); figure reprinted from Rothe *et al.* (2007*b*), with permission from the American Institute of Physics; copyright 2007.

peak and the appearance of a shoulder adjacent to the carboxyl peak (arrows) indicate complex formation. This behaviour has also been described for various polyvalent metal cations such as Eu(III), Tb(III) or UO_2^{2+} (Plaschke *et al.*, 2005). In the case of Zr(IV)–PAA, the shoulder becomes more pronounced at pH 3. It is plausible that at pH 5, where Zr(IV) hydrolysis and oxo/hydroxide formation is dominant (Cho *et al.*, 2005), PAA is merely coating and co-precipitating with these inorganic particles; no specific metal organic interaction is discernible from the C 1s-NEXAFS. This is corroborated by Zr *K*-EXAFS measurements (not shown), giving evidence for Zr(IV) hydrolysis product colloid formation under these conditions. Decreasing the pH leads to an increased fraction of ionic Zr(IV) which can be complexed by PAA carboxyl groups. This reaction seems to be more favourable at pH 3, indicated by the stronger complexation effect on the shoulder in the C 1s-NEXAFS. That this shoulder observed in the PAA spectrum results from a specific metal ion interaction with carboxyl functional groups is corroborated by quantum chemical calculations (see §3.2).

Turning now to metal cation/HA interaction, we have observed that HA aggregation induced by addition of polyvalent metal cations is generally accompanied by segregation into fractions with different X-ray optical densities in the STXM micrographs (Plaschke *et al.*, 2004, 2005). Both dense or 'dark' and less dense or 'light' zones possess characteristic C 1s-NEXAFS signatures. The segregation into different HA fractions induced by Zr(IV) is depicted in Fig. 5. Confined dark patches (one marked II in Fig. 5) are embedded into a lighter matrix of carbonaceous material (I). The corresponding C 1s-NEXAFS signatures are compared in Fig. 6, revealing differences in chemical composition between the two zones. In addition to the aromatic peak at ∼285 eV, the spectrum of the light zones (I) shows a distinct peak at ∼286.7 eV, attributed in the literature to phenolic carbon (Hitchcock *et al.*, 1992). The dominant carboxyl peak is observed at 288.4 eV. Interestingly, HA aggregates precipi-
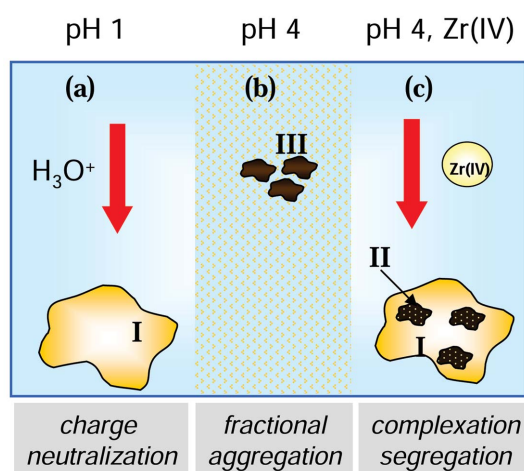
tated at pH 1 without addition of metal cations exhibit a spectral signature (not shown) similar to signature I derived from the 'light' zones. Averaging the spectroscopic signal over a full Zr(IV)–HA aggregate floc forming at pH 4 yields spectrum I. The spectrum of the dark zones (signature II) thus obviously characterizes a minority fraction. The dark areas also exhibit a less intense aromatic peak and a shoulder on the low energy side of the pronounced carboxyl resonance. This shoulder resembles the complexation feature observed for Zr(IV)–PAA at pH 3–4. Spectrum III in Fig. 6 was extracted from HA precipitated at around pH 4, without addition of metal cations. Note that this spectrum resembles the signature of the dark zones, with the exception that the shoulder preceding the carboxyl peak is missing.
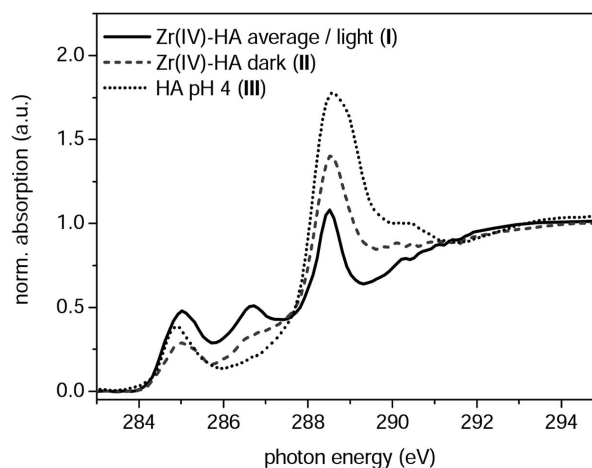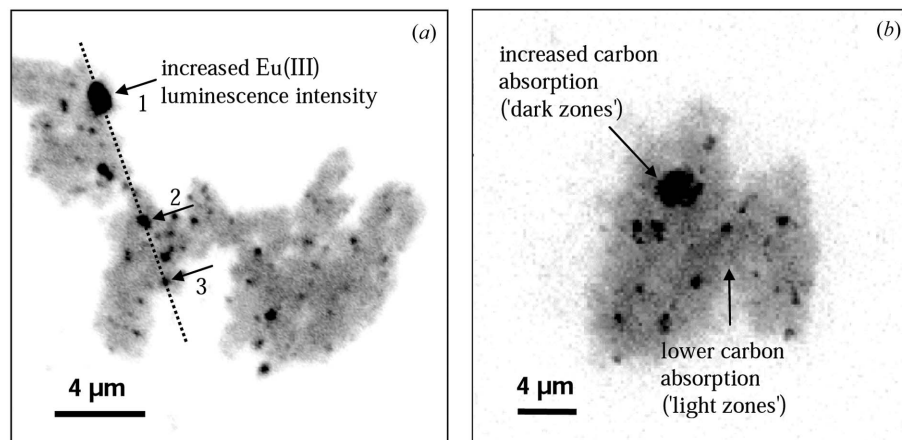

Figure 6
Normalized C 1s-NEXAFS recorded for HA at pH 4 (III) and Zr(IV)–HA fractions at pH 4 after metal cation induced aggregation and segregation ([Zr(IV)] = 1.1 × 10⁻³ mol l⁻¹; I and II refer to the light and dark zones indicated in Fig. 5, respectively); figure reprinted from Rothe *et al.* (2007*b*), with permission from the American Institute of Physics; copyright 2007.

soil and geosciences

To explain these effects [which are also observed for Eu(III)–HA, UO_2^{2+}–HA and other systems], we propose a simple mechanistic model of the M^{n+}/HA interaction (Rothe *et al.*, 2007a), schematically illustrated in Fig. 7. At low pH (*a*) protonation leads to HA precipitation *via* charge neutralization and subsequent agglomeration. The C 1s-NEXAFS (not shown but similar to signature I) is characteristic of the HA majority fraction rich in aromatic and phenolic subunits. At pH 4 (*b*), this fraction is dissolved, leaving behind a less soluble fraction exhibiting signature III. Saturating the HA loading capacity by adding metal cations, *e.g.* Zr(IV) at pH 4, leads to complexation and segregation (*c*). The dark zones (signature II) can be associated with the pH 4 minority fraction rich in carboxyl groups. It has a stronger affinity for metal cations, which will be shown below in the discussion of the LSLM results obtained for Eu(III)–HA. The corresponding C 1s-NEXAFS (signature II) exhibits a significant shoulder associated with a strong complexation reaction. The light zones represent the majority fraction aggregating due to M^{n+} charge neutralization, similar to charge neutralization through protonation at pH 1 (signature I).

In Fig. 8, LSLM and STXM micrographs of Eu(III)–HA aggregates are compared. Although similar at first glance, the contrast mechanism in these images is based on different physical processes, *i.e.* specific C 1s-level X-ray absorption (STXM) and optical Eu(III) luminescence emission (LSLM)

Figure 8

Comparison of (*a*) Eu(III) luminescence intensity distribution in Eu(III)–HA by LSLM (excitation wavelength 393.5 nm) and (*b*) specific carbon absorption by STXM (recorded at 288.4 eV) of Eu(III)–HA aggregates; confined patches with increased Eu(III) luminescence intensity or carbon absorption are marked with arrows; figure reprinted from Naber *et al.* (2006), with permission from Elsevier.

(Naber *et al.*, 2006). In the STXM image dark areas correlate with increasing optical density of the carbonaceous material. Dark areas in the LSLM image correlate with increased Eu(III) luminescence intensity ($^5D_0 \rightarrow {}^7F_{1,2}$ transitions). Both microscopy techniques reveal similar aggregate morphologies: confined dark patches (with diameters ranging from 200 nm to 2 µm) embedded in a lighter matrix. Although STXM and LSLM cannot be applied at the same time to the same sample, we may safely assume that zones with high optical density in the STXM image correlate with high Eu(III) luminescence intensities in the LSLM images. Therefore, we conclude that the metal cations are enriched in these zones. The intensity line profile of the Eu(III) luminescence extracted along the dashed line in Fig. 8(*a*) (not shown) indicates that most of these patches exhibit a three- to four-fold higher Eu(III) luminescence intensity compared with that of the surrounding matrix. This corresponds well to the three to four times higher carbon absorption detected for the dark zones compared with the light zones in the STXM micrographs.

In order to discriminate contributions from HA and the complexed Eu(III) cations to the total LSLM luminescence yield we have applied different emission filters with the centre wavelength set to the organic HA luminescence emission (565 nm) and the two dominant Eu(III) emission lines at 592 nm and 615 nm, respectively (Plaschke *et al.*, 2009). The corresponding LSLM images are depicted in Figs. 9(*b*)–9(*d*). The image without emission filters is shown in Fig. 9(*a*). In these images, lighter regions correspond to areas of higher luminescence intensity. The dashed line in Fig. 9(*a*) transverses a strongly luminescent spot (circled area), corresponding to the dense zones in the STXM micrographs, and a region of less luminescent matrix, corresponding to the lighter zones in the STXM micrographs. The fluorescence intensities along this line are depicted in Figs. 9(*e*)–9(*h*) for the different filter settings. Coarse spectral information for these two sample regions can be derived from the integrated peak intensities
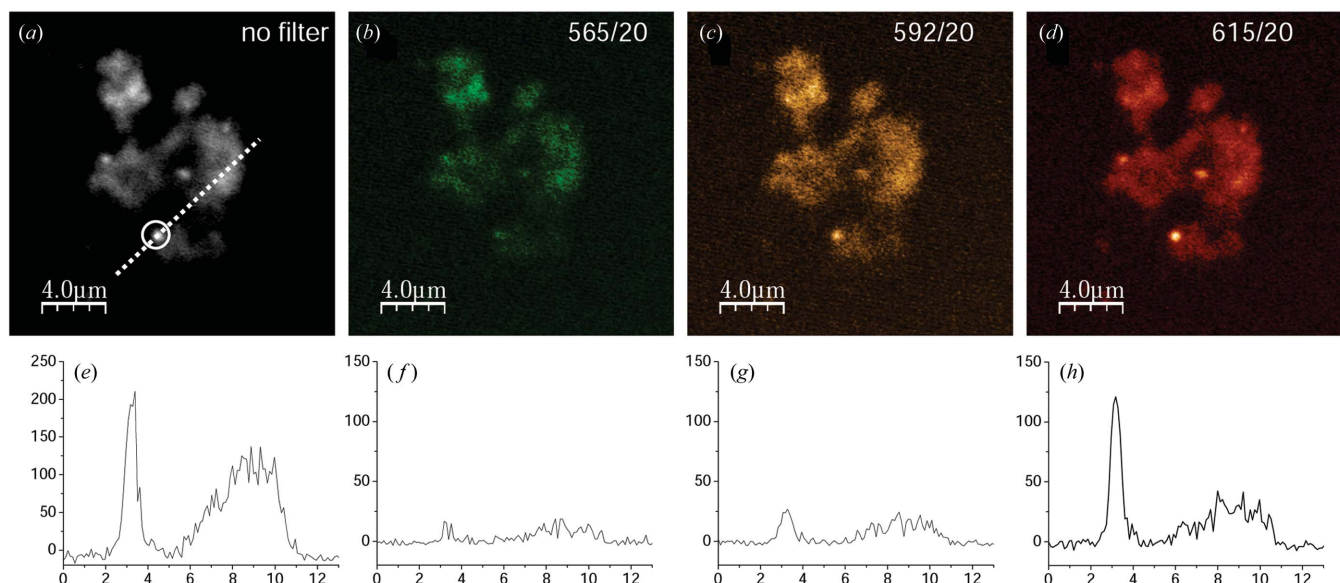

Figure 7

Mechanistic model describing HA precipitation *versus* fractionation under various pH conditions and following metal cation complexation. Signatures I–III correspond to spectra in Fig. 6. Note that useful C 1s-NEXAFS spectra can only be derived from flocculated material and not from dissolved HA fractions (see text for details); figure reprinted from Rothe *et al.* (2007b), with permission from the American Institute of Physics; copyright 2007.

Figure 9
(a)–(d) LSLM images of a Eu(III)–HA aggregate at pH 5 [(a) recorded without emission filter and (b)–(d) filters set to 565, 592 and 615 nm, FWHM 20 nm] and (e)–(h) the corresponding fluorescence intensities (y-axis, a.u.) as line profiles (x-axis, μm) along the dashed line in (a), see text for details; figure reprinted from Plaschke et al. (2009), with permission from IOP Publishing.

obtained with the different filter settings. The generally weak luminescence signal at 565 nm (Fig. 9b) corresponds to organic HA fluorescence. The $^5D_0 \rightarrow {}^7F_2$ transition ('hypersensitive band') at 615 nm is known to indicate changes in the Eu(III) coordination geometry. This transition gains intensity upon complex formation (Fig. 9h), while the adjacent $^5D_0 \rightarrow {}^7F_1$ transition is not affected by complexation (Fig. 9g). We have observed that the intensity ratio $^5D_0 \rightarrow {}^7F_2$ (615 nm)/$^5D_0 \rightarrow {}^7F_1$ (592 nm) is strongly increased in the dense, highly luminescent zones compared with the light, less luminescent zones. Hence, spatially resolved LSLM intensity ratios of the dominant Eu(III) emission lines point to different complexation mechanisms or strengths in X-ray optically dense and light zones.

3.2. Quantum chemical calculations

Spectroscopic properties derived from quantum chemical calculations depend on the topology of a molecule, i.e. type of atoms, distances and angles between them. The knowledge of well defined structural parameters allows calculation of the quantum mechanical wavefunctions, energy expectation values and response properties of molecular systems. Organic acids with comparably simple molecular structure can be successfully treated with moderate computational effort, as previously demonstrated for various substituted benzoic acids (Bâldea et al., 2007). Both PAA and HA are organic macromolecules with an ill-defined (PAA) or even unknown (HA) molecular topology. Nevertheless, as mentioned above, carboxyl groups are known to be the primary complexing sites for metal cations in these organic substances. Therefore, quantum chemical calculations were performed for three different hydrated mono-acetate complexes having different coordination geometries for trivalent cations La(III), Eu(III),

Gd(III), Cm(III), tetravalent Zr(IV) and uranyl (UO_2^{2+}). These were considered as models for the bonding environment in HA and PAA complexes. For these systems the carboxylic C 1s (COO^-) $\rightarrow \pi^*_{C=O}$ transition in the metal ion acetate complexes was calculated ab initio and compared with that for the free acetate ion using the RI-ADC(2) approach implemented in the TURBOMOLE program package (Armbruster et al., 2009).

For various metal cations the calculated spectra of acetate complexes show a complexation shift, Δf, of the C 1s (COO^-) $\rightarrow \pi^*_{C=O}$ transition to lower energies compared with calculated energy for the free acetate anion (Fig. 10). The theoretically calculated excitation energies are given as calculated by the RI-ADC(2) approach and are not shifted to coincide with experimental values. Computed Δf values are within the same range as experimentally determined values for the difference in energy between the C 1s (COO^-) $\rightarrow \pi^*_{C=O}$ peak and the shoulder observed following complexation in C 1s NEXAFS spectra of PAA/M^{n+}–PAA systems. The computations reveal that structural modifications of the ligand following metal cation complexation determine the magnitude of Δf, with only small contributions affected by metal centre electronic structure or hydration. Although the calculation of C 1s core excitation spectra of complex organic macromolecules (PAA or HA) is not yet possible with currently available quantum chemical methods, selected spectral features can be reproduced for structurally well defined subunits. As calculated Δf values for metal ion acetates (in the range 0.44–1.02 eV) correspond well to the experimental values obtained for PAA/M^{n+}–PAA (in the range 0.5–1 eV) we conclude that calculations of carboxyl transitions in metal acetates at the ab initio level provide further evidence for the correct interpretation of the experimentally observed C 1s-NEXAFS absorption feature as a complexation effect in PAA and HA. The feature
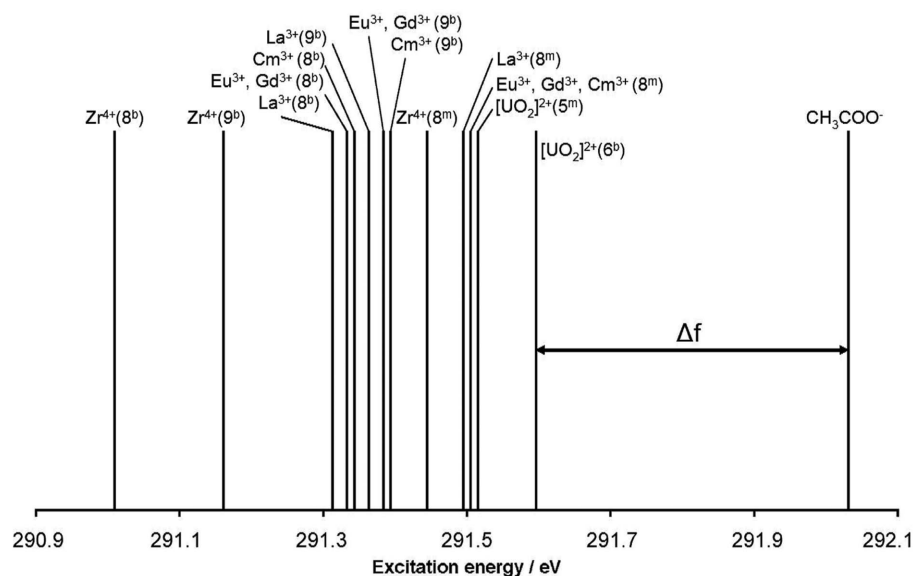
Figure 10
The C 1s (COO$^-$) $\rightarrow$ $\pi^*_{C=O}$ transition energies in eV obtained for different structures and metal cations by RI-ADC(2) calculations. The numbers after the element symbols represent the coordination numbers; superscripts b and m correspond to the bi- and monodentate acetate bonding, respectively; figure reprinted from Armbruster *et al.* (2009), with permission from Elsevier.

observed 0.5–1 eV below the carboxyl resonance of the organic acid can be attributed to an energy shifted 1$s \rightarrow \pi^*_{C=O}$ transition in the M^{n+}/carboxylic acid complex. This implies that the decrease in organic acid carboxyl resonance intensity upon complexation with M^{n+} occurs because this transition splits into two features and a portion of its original intensity becomes associated with the new lower energy transition. Moreover, the calculations show that the extent of the energy shift is primarily dependent on the binding mode of the carboxylate groups to the metal centres, bidentate *versus* monodentate, and on structural parameters of the ligand itself.

4. Conclusions

The combination of two spectromicroscopy methods probing the organic ligand (STXM/C 1s-NEXAFS) and the metal centre (LSLM/luminescence spectroscopy) has given further evidence for the existence of chemically different fractions in HA. The STXM results allowed us to identify different HA fractions interaction with metal cations by their optical densities and spectral fingerprints. However, we could only localize the metal cations associated with these fractions from ancillary LSLM information. Note that comparative investigations of well defined reference systems and quantum chemical calculations to provide a foundation for sound interpretation of spectral features were indispensable for the interpretation of spectroscopic results obtained in HA/metal cation interaction experiments. Our experiments have shown that M^{n+} bound to HA are enriched and/or more strongly bound in a minority fraction containing higher densities of complexing carboxylic sites. This fraction is likely to play a dominant role in HA colloid mediated transport of toxic trace metals in the hydrosphere. Macroscopic properties attributed

to HA, including cation loading capacities and complexation constants, must be treated as averaged empirical values. These values are not sufficient for the detailed understanding of the underlying molecular processes. The present study points to the necessity to establish and further develop spatially resolved spectroscopic techniques to investigate inherently inhomogeneous natural samples. Through such developments our understanding of the HA fractions and their binding to metal cations may become refined.

References

Armbruster, M. K., Schimmelpfennig, B., Plaschke, M., Rothe, J., Denecke, M. A. & Klenze, R. (2009). *J. Electron Spectrosc. Relat. Phenom.* **169**, 51–56.

Bâldea, I., Schimmelpfennig, B., Plaschke, M., Rothe, J., Schirmer, J., Trofimov, A. B. & Fanghänel, Th. (2007). *J. Electron Spectrosc. Relat. Phenom.* **154**, 109–118.

Bluhm, H. *et al.* (2006). *J. Electron Spectrosc. Relat. Phenom.* **150**, 86–104.

Christl, I. & Kretzschmar, R. (2007). *Environ. Sci. Technol.* **41**, 1915–1920.

Cho, H.-R., Walther, C., Rothe, J., Neck, V., Denecke, M. A., Dardenne, K. & Fanghänel, Th. (2005). *Anal. Bioanal. Chem.* **383**, 28–40.

Denecke, M. A., Reich, T., Pompe, S., Bubner, M., Heize, K.-H., Nitsche, H., Allen, P. G., Bucher, J. J., Edelstein, N. M., Shuh, D. K. & Czerwinski, K. R. (1998). *Radiochim. Acta*, **82**, 103–108.

Hayes, M. H. B. (1989). *Humic Substances II*, edited by P. MacCarthy, R. L. Malcolm and R. S. Swift. New York: John Wiley.

Hitchcock, A. P., Urquhart, S. G. & Rightor, E. G. (1992). *J. Phys. Chem.* **96**, 8736–8750.

Jacobsen, C., Flynn, G., Wirick, S. & Zimba, C. (2000). *J. Microsc.* **197**, 173–184.

Jacobsen, C., Williams, S., Anderson, E., Browne, M. T., Buckley, C. J., Kern, D., Kirz, J., Rivers, M. & Zhang, X. (1991). *Opt. Commun.* **86**, 351–364.

Kaznatcheev, K. V., Karunakaran, ch., Lanke, U. D., Urquhart, S. G., Obst, M. & Hitchcock, A. P. (2007). *Nucl. Instrum. Methods Phys. Res. A*, **582**, 96–99.

Kim, J. I. (1994). *MRS Bull.* **19**, 47–56.

Kim, J. I., Buckau, G., Li, G. H., Duschner, H. & Psarros, N. (1990). *Fresenius J. Anal. Chem.* **338**, 245–252.

Kim, J. I. & Czerwinski, K. R. (1996). *Radiochim. Acta*, **73**, 5–10.

Monsallier, J.-M., Artinger, R., Denecke, M. A., Scherbaum, F. J., Buckau, G. & Kim, J. I. (2003). *Radiochim. Acta*, **91**, 567–574.

Monsallier, J.-M., Scherbaum, F. J., Buckau, G., Kim, J. I., Kumke, M. U., Spechi, C. H. & Frimmel, F. H. (2001). *J. Photochem. Photobiol. A*, **138**, 55–63.

Myneni, S. C. B. (2002). *Reviews in Mineralogy and Geochemistry*, Vol. 49, *Application of Synchrotron Radiation in Low-Temperature Geochemistry and Environmental Science*, edited by P. A. Fenter, M. L. Rivers, N. C. Sturchio and S. R. Sutton, p. 485. Washington: Geochemical Society and Mineralogical Society of America.

Naber, A., Plaschke, M., Rothe, J., Hofmann, H. & Fanghänel, Th. (2006). *J. Electron Spectrosc. Relat. Phenom.* **153**, 71–74.

Neuhäusler, U., Jacobsen, C., Schulze, D., Stott, D. & Abend, S. (2000). *J. Synchrotron Rad.* **7**, 110–112.

Plaschke, M., Rothe, J., Altmaier, M., Denecke, M. A., Fanghänel, Th. (2005). *J. Electron Spectrosc. Relat. Phenom.* **148**, 151–157.

Plaschke, M., Rothe, J., Denecke, M. A. & Fanghänel, Th. (2004). *J. Electron Spectrosc. Relat. Phenom.* **135**, 53–62.

Plaschke, M., Rothe, J., Klenze, R., Wissler, J. & Naber, A. (2009). *J. Phys. Conf. Ser.* **186**, 012094.

Rothe, J., Plaschke, M. & Denecke, M. A. (2007b). In *X-ray Absorption Fine Structure – XAFS13*, edited by B. Hedmann & P. Pianetta. New York: American Institute of Physics.

Rothe, J., Plaschke, M., Schimmelpfennig, B. & Denecke, M. A. (2007a). In *Speciation Techniques an Facilities for Radioactive materials and Synchrotron Light Sources*. Issy-les-Moulineaux: Nuclear Energy Agency.

Thieme, J., Schmidt, C., Abbt-Braun, G., Specht, C. & Frimmel, F. H. (2000). In *Refractory Organic Substances in the Environment*, edited by F. H. Frimmel and G. Abbt-Braun. New York: Wiley.

Tzvetkov, G., Graf, B., Wiegner, R., Raabe, J., Quitmann, C. & Finck, R. (2008). *Micron*, **39**, 275–279.